

A Search for Boron in Damped Ly α Systems

Trystyn A. M. Berg¹, Sara L. Ellison¹, Kim A. Venn¹, J. Xavier Prochaska²

¹ *Department of Physics and Astronomy, University of Victoria, Victoria, British Columbia, V8W 2Y2, Canada.*

² *Department of Astronomy and Astrophysics, University of California, Santa Cruz, Santa Cruz, CA, 95064, USA.*

20 November 2021

ABSTRACT

We present the first systematic study of boron beyond the Local Group. This analysis is performed on a sample of 30 damped Ly α systems (DLAs) with strong metal-lines, which are expected to trace the interstellar medium of high z galaxies. We report on two boron detections at $> 3\sigma$ significance; one new detection and one confirmation. The ratios of B/O and, for the first time, B/S are compared with previous stellar and interstellar measurements in the Milky Way and Small Magellanic Cloud. The novel comparison with sulphur, which tracks oxygen’s abundance, alleviates the uncertainty associated with stellar oxygen measurements. For both detections, the inferred B/S ratio is in excess of the prediction of primary boron production from spallation processes. Possible sources of contamination are discussed, as well as physical effects that could impact the observed ratios. However taken at face value, the implication of these measurements suggest potentially higher cosmic ray fluxes in DLAs. The prospects for future boron detections in other high redshift DLAs to confirm our results is also discussed.

Key words: galaxies: abundances – galaxies: high redshift – galaxies: ISM – quasars: absorption lines

1 INTRODUCTION

Although most elements are primarily formed through stellar or Big Bang nucleosynthesis, beryllium and boron are notable exceptions. Reeves et al. (1970) first described Be and B formation through the spallation of galactic cosmic rays (GCRs) with CNO nuclei. The original picture of Be and B production from spallation involved interstellar protons and alpha particles that are accelerated by supernovae and which subsequently collide with interstellar CNO. The production of B and Be through this *forward* mechanism (also known as *direct* spallation) depends on both the rate of GCR production (i.e. supernova rate) and on the metallicity of the interstellar medium (ISM). Forward spallation is therefore considered to be a *secondary* process with a predicted dependence of Be and B $\propto [\text{CNO}]^2$ (i.e. $m = 2$ where m is the slope of the logarithmic dependence between Be and B with CNO).

However, the simple model of forward spallation is in conflict with the metallicity-independent production of the light elements which is observed in halo stars (e.g. Duncan et al. 1992; Boesgaard et al. 1999a). Models of B and Be production have therefore tried to identify *primary* mechanisms (Be, B $\propto [\text{CNO}]$, $m = 1$) such as the ν -process in stars (Woosley et al. 1990), or spallation in which the GCRs always have the same CNO content (Duncan et al. 1992). The latter class of processes is referred to as *reverse* spal-

lation and generally entails the acceleration of CNO nuclei which then collide with ambient protons or alpha particles. Various mechanisms have been suggested to accomplish reverse spallation, including supernovae accelerating either 1) their own ejecta, 2) locally enriched superbubble material or 3) wind-enriched material around massive rotating stars (see Prantzos 2012, for a review). In reality, there may be multiple processes that contribute to Be and B production, where an intuitive combination may be one where reverse spallation (with interstellar protons and alpha particles as the targets) dominates in a metal-poor ISM. As the ISM enriches and more CNO targets accumulate, forward spallation can become more effective. Quantifying the relative contributions of different processes requires detailed chemical modeling which can simultaneously account for the observed abundances of B, Be and Li (which can also be produced through spallation), as well as isotopic ratios (Fields et al. 2000; Prantzos 2012).

Meanwhile, observational studies of boron are quite limited. The strongest boron transitions required for determining stellar abundances are situated in the ultra-violet (UV) and have very weak oscillator strengths. Furthermore, boron astration due to rotational mixing in stars also impacts measurements (Venn et al. 2002; Mendel et al. 2006).

In addition to the observational challenge of measuring boron, a further complication for the interpretation of boron

(and Be) abundances is the comparison with the oxygen abundance (e.g., Fields et al. 2000). Despite its high cosmic abundance and variety of spectral features available for measurement, determining accurate O/H abundances has been a subject of much controversy (e.g., Boesgaard et al. 1999b; Israelian et al. 2001, and references therein). In brief, there are four different features that are commonly used for determining oxygen abundances (the [OI] $\lambda\lambda 6300, 6363$ Å forbidden lines, near infra-red (IR) OH vibration-rotation $\lambda\lambda 1.6, 3.4$ μm lines, the UV OH $\lambda 3100\text{-}3200$ Å lines, and the OI triplet at $\lambda 7771\text{-}7775$ Å) yet they result in internally inconsistent abundances. Specifically, the UV OH lines tend to find a rising [O/Fe] at low [Fe/H], in contrast with an [O/Fe] plateau from [OI] measurements (e.g. Kraft et al. 1992; Carretta et al. 2000). It is clear that the uncertainty in oxygen abundances complicates both the direct comparisons of Be and B with O, but also hinders observational studies that rely on converting Fe to O via calibrated relative abundances. For example, the boron study of Smith et al. (2001) attempted to derive oxygen abundances in halo stars from Fe measurements taken from Duncan et al. (1997) and Garcia Lopez et al. (1998). To convert from Fe to O, three different models were applied to describe [O/Fe] as a function of [Fe/H], representing the uncertainty in the conversion. Depending on the choice of conversion, they determined a dependence of B on O that ranged from purely primary ($m=0.92, 1.05$), to a mix of primary and secondary processes ($m=1.44$). An accurate interpretation of Be and B production mechanisms clearly requires a reliable oxygen (or proxy) abundance.

Despite these challenges, observations of Be and B in stars have been used to infer that their production is a combination of both primary and secondary processes. Smith et al. (2001) determined oxygen abundances from the weak [O I] lines for 13 F and G field stars for which Cunha et al. (2000) derived the boron abundances. The best-fit slope of the B-O relation was found to be $m = 1.39$, suggesting a combination of primary and secondary processes. This agrees with an analysis of beryllium done by Rich & Boesgaard (2009), who observed 24 stars and compared the best-fit double power model ($[\text{O}/\text{H}] > -1.8$ and $[\text{O}/\text{H}] < -1.4$; $m = 1.59, 0.74$ respectively) and a single line best fit ($m = 1.21$) of their Be-O relation. They found that there appeared to be a two-component trend with a break point at $[\text{O}/\text{H}] \sim -1.6$ ($[\text{Fe}/\text{H}] \sim -2.2$), indicating a transition from primary to secondary processes.

Interstellar boron can also contribute to our understanding of its origin, although relatively few observational studies exist. The first observation of interstellar boron was made by Meneguzzi & York (1980) using the Copernicus satellite. However, it was the launch of the Hubble Space Telescope (HST) that allowed real progress in this area with observations made first with the Goddard High Resolution Spectrograph (GHRS) (Federman et al. 1993; Jura et al. 1996), and later with the Space Telescope Imaging Spectrograph (STIS) (Howk et al. 2000). Importantly, Howk et al. (2000) found that boron can be significantly depleted onto dust in the ISM, leading to potential under-estimates of its actual abundance. They found that boron is more easily depleted in the cold diffuse ISM, and demonstrated an anti-correlation of the boron abundance with hydrogen gas density. The most recent measurements of interstellar boron have been made by Ritchey et al. (2011) who added a fur-

ther 56 Galactic sight-lines observed with STIS. Based on their sight-lines through warm, low density gas (assumed to be relatively undepleted) Ritchey et al. (2011) determine an ISM abundance of $\text{B}/\text{H} = 2.4 \pm 0.6 \times 10^{-10}$, agreeing with the results from undepleted B-type stars (Venn et al. 2002) and previous ISM studies (Howk et al. 2000).

Beyond the stellar and interstellar measurements in the Milky Way, there has been only one extra-Galactic study of boron. Brooks et al. (2002) observed two B-type stars in the Small Magellanic Cloud (SMC) in an attempt to compare boron production relative to the Milky Way. The two boron upper limits presented by Brooks et al. (2002) lie below the expectation for primary boron production, but are consistent with a secondary production mechanism. However, Brooks et al. (2002) acknowledge that their measurements do not account for depletion of boron due to rotational mixing, hence they suggest that their limits do not necessarily rule out primary production.

The interpretation of boron abundances in other galaxies depends on both the cosmic ray flux (CRF) and the abundance of spallation targets. The SMC has an oxygen abundance around one quarter of that in the solar neighbourhood (Korn et al. 2000; Salmon et al. 2012), and 15% of its current CRF (based on Fermi/Large Area Telescope (LAT) gamma ray observations of the SMC, see Abdo et al. 2010; Sreekumar et al. 1993). Brooks et al. (2002) point out that the lower oxygen abundance and cosmic ray flux in the SMC might be expected to have a compound effect that leads to a production of boron of that is $\sim 1/20$ lower than the solar neighbourhood for secondary boron production, but also discuss the effect of higher past star formation rates and CRF confinement times. The discussion in Brooks et al. (2002) reveals that high boron abundances that exceed the primary dependence (i.e. $[\text{B}/\text{H}] > [\text{O}/\text{H}]$) can indicate high cosmic ray fluxes, which in turn may be related to high rates of star formation. The study of boron in other galaxies therefore provides a novel approach to constraining their star formation histories.

To study boron in other galaxies, and in particular, to push to higher redshifts, damped Lyman alpha systems (DLAs) offer a plausible prospect. DLAs are quasar absorption line systems defined to have a column density of HI of $N(\text{HI}) \geq 2 \times 10^{20}$ atoms cm^{-2} , and have been widely used to study the chemistry of high z galaxies (e.g., see the review by Wolfe et al. 2005). Conveniently for the present study, their cosmological distances provide the advantage of observing the redshifted B II $\lambda 1362$ line in the optical, avoiding the use of space-based telescopes which currently limits Galactic boron observations.

Due to the weakness of the B II $\lambda 1362$ line, the most promising first targets for boron observations in DLAs will be absorbers with relatively strong metal lines. A sample of such absorbers has been assembled by Herbert-Fort et al. (2006), who studied the so-called metal-strong DLAs (MS-DLAs), defined to have metal column densities $\log N(\text{ZnII}) \geq 13.15$ and $\log N(\text{SiII}) \geq 15.95$. The possibility of boron detection in MSDLAs has been demonstrated by a tentative detection in the proto-typical MSDLA FJ0812+3208 ($z_{\text{abs}}=2.626$, $\log N(\text{HI})=21.35$) by Prochaska et al. (2003b).

In this paper, we present the first systematic search for boron in DLAs. We present a sample of 30 DLAs that have been selected as promising targets for boron detection based

on either the strength of their metal lines, or overall metallicity. A further novelty of our study is that, for the first time in a boron study, we consider sulphur as a proxy for oxygen to circumvent the problem with absolute oxygen abundances described above. The substitution of sulphur for oxygen has been frequently used in DLAs, both for consistency in comparisons with Galactic stellar data (Nissen et al. 2004, 2007) and because the oscillator strengths of the OI transitions often precludes an oxygen abundance determination (Pettini et al. 2002). Although both are alpha capture elements, it should be emphasized they do not have the same nucleosynthetic origin. Oxygen is primarily a product of helium and neon burning in massive stars, whereas sulphur is produced in oxygen burning and alpha-rich freezeout of core collapse supernovae (Woosley & Weaver 1995). We therefore explicitly test the substitution of sulphur for oxygen. High resolution echelle spectra have been obtained for each of the 30 target DLAs and measurements (or limits) made for the abundances of oxygen, boron and sulphur. The sample includes additional data for FJ0812+3208, increasing the spectral signal-to-noise (S/N) and permitting a re-analysis of this system.

2 TARGETS OF OBSERVATION

2.1 Sample Description

Boron is an intrinsically rare element with a solar abundance one million times less than oxygen. As a result of boron's low abundance and small oscillator strengths, it has intrinsically weak singly ionized lines. We have therefore selected a sample of 30 DLAs that is biased towards the most metal-rich DLAs, or those whose metal lines are very strong due to high N(HI) column densities (see Table 1). Many of the objects were selected based on low-resolution spectra that indicated the possibility of high metallicities (see Kaplan et al. 2010). A further benefit of the typically high metallicities of our sample is that the DLAs span the metallicity range of the stars in which boron has been observed so far in the Milky Way, facilitating a comparison between the two populations.

The sample consists of 19 MSDLAs (selected purely on the basis of their metal line strengths) and 11 DLAs with relatively high abundances. Metallicities for our sample were determined according to the scheme laid out by Rafelski et al. (2012) where the assumed metallicity is the abundance of either sulphur, silicon, zinc, or iron¹ (in order of decreasing preference). Metallicities of our sample along with the element used are tabulated in Table 2. The sample spans a wide range in N(HI) and specifically targets the metal-rich end of the literature sample presented by Rafelski et al. (2012). To emphasize this, Figure 1 shows the distribution of metallicity ([M/H]; left), and hydrogen column density (N(HI); right) relative to the literature sample of 195 DLAs ($z = 0.091$ – 4.743 Rafelski et al. 2012). The left panel shows that higher metal contents are probed in our sample, along with a range of hydrogen column densities.

2.2 Observations and Data Reduction

All of the observations presented here have been made using the High Resolution Echelle Spectrometer (HIRES) spectrograph on the Keck I telescope. Table 1 lists the QSOs that have been observed, exposure time and the S/N ratio (per pixel) near to the BII λ 1362 Å line (see Section 3).

The majority of data were taken with the HIRES spectrometer configured with the blue cross-disperser and the C1 decker giving a FWHM spectral resolution of $\approx 6 \text{ km s}^{-1}$. The CCD was binned spatially by 2 and the spectra were optimally extracted to a fixed dispersion of 1.3 km s^{-1} per pixel. Complete details on these observations will be presented in a future work (Berg et al., in prep.). The spectra were reduced using the XIDL code² following standard techniques. The HIREDUX software was used to reduce the spectra, and was fitted using the X_CONTINUUM routine which fits the continuum order by order before converting into a 1D spectrum.

¹ A +0.3 dex correction is included for iron to account for dust depletion.

² <http://www.ucolick.org/~xavier/IDL>

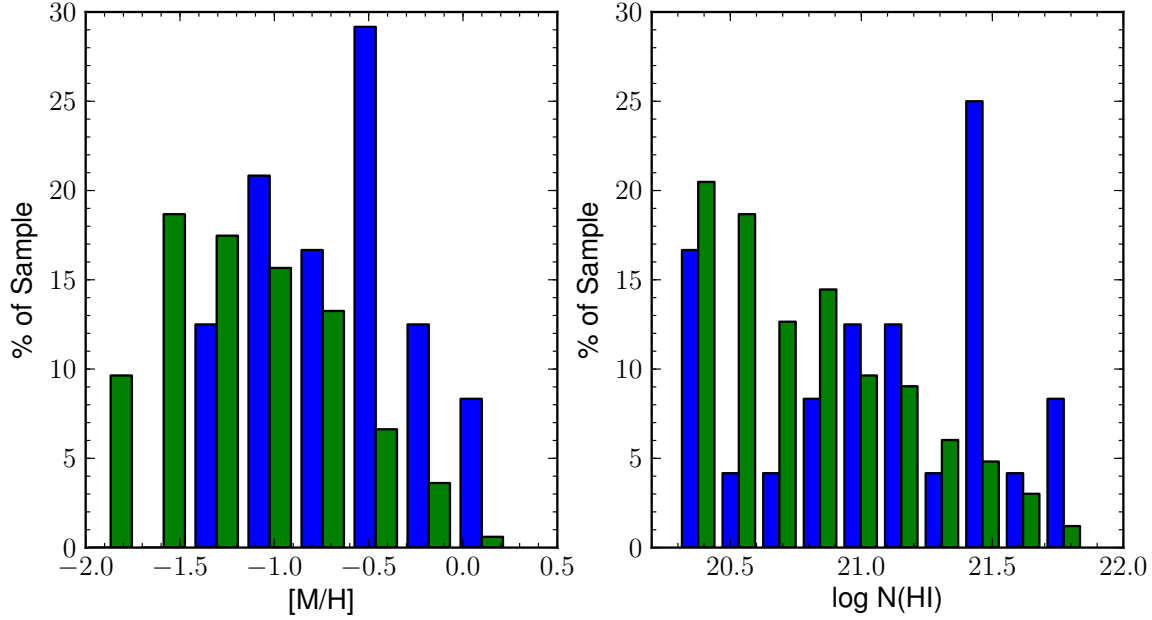


Figure 1. Distribution of metallicity ($[M/H]$; *left*), and hydrogen column density ($N(\text{HI})$; *right*). The literature sample from Rafelski et al. (2012) is plotted in green, and our metal-rich sample is plotted in blue. Note that absorbers without a measured hydrogen column density are excluded from the histograms.

Table 1. Target List

Quasar	R.A.	Dec.	Magnitude (band)	Exposure Time (s)	S/N_{1362}^a (pixel $^{-1}$)	MSDLA?
J0008−0958	00:08:15.3	−09:58:54.0	18.4 (r)	15029	11	Yes
J0058+0115	00:58:14.3	+01:15:30.2	17.7 (r)	14400	23	No
Q0201+36	02:04:55.6	+36:49:18.0	17.5 (r)	24980	...	No
Q0458−02	05:01:12.8	−01:59:14.2	19.0 (R)	28800	4	Yes
FJ0812+3208	08:12:40.7	+32:08:08.6	17.5 (r)	40500	45	Yes
J0927+1543	09:27:59.8	+15:43:21.8	18.8 (r)	12800	4	Yes
J0927+5823	09:27:08.8	+58:23:19.4	18.3 (r)	21600	14	No
J1010+0003	10:10:18.2	+00:03:51.3	18.1 (r)	7200	1	No
J1013+5615	10:13:36.4	+56:15:36.4	18.5 (r)	3600	5	Yes
J1049−0110	10:49:15.4	−01:10:38.1	17.8 (r)	4800	13	No
J1056+1208	10:56:48.7	+12:08:26.8	17.9 (r)	21300	18	Yes
J1155+0530	11:55:38.6	+05:30:50.6	18.1 (r)	7200	10	No
J1159+0112	11:59:44.8	+01:12:07.0	17.3 (r)	25000	22	Yes
J1200+4015	12:00:39.8	+40:15:56.0	18.3 (r)	10800	13	Yes
J1249−0233	12:49:24.9	−02:33:39.7	17.7 (r)	7300	10	Yes
J1310+5424	13:10:40.2	+54:24:49.6	18.5 (r)	10800	11	Yes
J1313+1441	13:13:41.9	+14:41:40.5	18.2 (r)	10200	9	Yes
J1417+4132	14:17:19.2	+41:32:37.0	18.4 (r)	25200	30	No
J1524+1030	15:24:30.1	+10:30:32.0	18.1 (r)	9000	6	Yes
J1552+4910	15:52:33.9	+49:10:08.3	18.0 (r)	9000	20	Yes
J1555+4800	15:55:56.9	+48:00:15.0	19.1 (r)	21600	6	Yes
J1604+3951	16:04:14.0	+39:51:21.9	18.1 (r)	10300	15	Yes
J1610+4724	16:10:09.4	+47:24:44.5	18.8 (r)	10800	8	Yes
Q1755+578	17:56:03.6	+57:48:48.0	18.3 (R)	30400	11	Yes
J2100−0641	21:00:25.0	−06:41:45.0	18.1 (r)	28000	28	Yes
J2222−0945	22:22:56.1	−09:46:36.0	18.0 (r)	10800	16	No
Q2230+02	22:32:35.3	+02:47:55.1	18.0 (R)	27600	7	No
J2241+1225	22:41:45.1	+12:25:57.1	17.9 (r)	7200	6	Yes
J2340−0053	23:40:23.7	−00:53:27.0	17.5 (r)	15000	23	No
Q2342+34	23:44:51.1	+34:33:46.8	19.1 (V)	7200	11	No

^a The S/N is quoted near the observed position of the BII $\lambda 1362$ line.

Table 2. Boron, Oxygen, and Sulphur Column Densities and Abundances

QSO	z_{em}	z_{obs}	$\log N(\text{HI})$	$\log N(\text{BII})$	$\log N(\text{SII})$	$\log N(\text{OI})$	[B/H]	[S/H]	[O/H]	[M/H]	M
J0008-0958	1.95	1.76753	20.85 ± 0.15 (1)	< 12.07	15.83 ± 0.02	< 18.03	< 0.43	-0.17 ± 0.15	< 0.49	-0.17 ± 0.15	S
J0058+0115	2.49	2.00953	21.10 ± 0.15 (1)	11.95 ± 0.04	15.41 ± 0.01	...	0.06 ± 0.16	-0.84 ± 0.15	...	-0.84 ± 0.15	S
Q0201+36	2.49	2.46280	20.38 ± 0.15 (2)	-0.35 ± 0.15	Si
Q0458-02	2.29	2.03950	21.65 ± 0.09 (3)	< 12.53	...	< 18.452	< 0.09	...	< 0.18	-1.10 ± 0.10	Zn
FJ0812+3208	2.71	2.62593	21.35 ± 0.15 (4)	11.43 ± 0.08	15.48 ± 0.02	< 17.69	-0.71 ± 0.17	-1.02 ± 0.15	< -0.35	-1.02 ± 0.15	S
J0927+1543	1.80	1.73113	...	< 12.96	< 15.86	< 18.97
J0927+5823	1.91	1.63515	20.40 ± 0.25 (2)	...	15.79 ± 0.14	< 18.33	...	0.24 ± 0.28	< 1.24	0.24 ± 0.28	S
J1010+0003	1.40	1.26514
J1013+5615	3.61	2.28400
J1049-0110	2.12	1.65760	20.35 ± 0.15 (1)	...	15.47 ± 0.01	< 18.11	...	-0.03 ± 0.15	< 1.07	-0.03 ± 0.15	S
J1056+1208	1.92	1.60954	21.45 ± 0.15 (2)	< 12.21	> 15.66	< 18.20	< -0.03	> -0.94	< 0.06	-0.32 ± 0.16	Zn
J1155+0530	3.48	3.32607	21.05 ± 0.10 (4)	< 12.02	15.35 ± 0.003	< 17.66	< 0.18	-0.85 ± 0.10	< -0.08	-0.85 ± 0.10	S
J1159+0112	2.00	1.94375	21.80 ± 0.10 (5)	< 12.04	> 15.16	...	< -0.55	> -1.79	...	-1.30 ± 0.11	Zn
J1200+4015	3.36	3.22000	20.65 ± 0.15 (4)	< 11.82	15.37 ± 0.01	< 17.79	< 0.38	-0.43 ± 0.15	< 0.45	-0.43 ± 0.15	S
J1249-0233	2.12	1.78085	21.45 ± 0.15 (6)	< 12.34	15.50 ± 0.02	< 18.23	< 0.10	-1.10 ± 0.16	< 0.09	-1.10 ± 0.16	S
J1310+5424	1.93	1.80070	21.45 ± 0.15 (2)	< 12.39	> 15.96	< 18.39	< 0.15	> -0.64	< 0.25	-0.51 ± 0.16	Zn
J1313+1441	1.88	1.79480	...	< 12.21	15.71 ± 0.01	< 18.19
J1417+4132	2.02	1.95090	21.45 ± 0.25 (6)	< 12.02	> 15.8	17.98 ± 0.07	< -0.22	> -0.80	-0.16 ± 0.26	-0.54 ± 0.25	Zn
J1524+1030	2.06	1.94094	...	< 12.13	> 15.53	< 18.05
J1552+4910	2.04	1.95987	...	< 11.95	15.34 ± 0.004	< 17.96
J1555+4800	3.30	2.39089	21.50 ± 0.15 (4)	...	> 15.88	> -0.77	...	-1.22 ± 0.20	Fe
J1604+3951	3.13	3.16400	21.75 ± 0.20 (4)	< 11.71	15.70 ± 0.04	< 17.69	< -0.83	-1.20 ± 0.20	< -0.75	-1.20 ± 0.20	S
J1610+4724	3.22	2.50661	21.00 ± 0.15 (4)	< 12.38	> 16.01	< 18.35	< 0.59	> -0.14	< 0.66	-0.08 ± 0.16	Zn
Q1755+578	2.11	1.97110	21.40 ± 0.15 (7)	< 11.91	> 15.97	< 17.88	< -0.28	> -0.57	< -0.21	-1.04 ± 0.15	Fe
J2100-0641	3.14	3.09130	21.05 ± 0.15 (4)	< 11.78	15.64 ± 0.002	< 17.71	< -0.06	-0.56 ± 0.15	< -0.03	-0.56 ± 0.15	S
J2222-0945	2.93	2.35430	20.55 ± 0.15 (4)	< 12.05	15.33 ± 0.02	...	< 0.71	-0.37 ± 0.15	...	-0.37 ± 0.15	S
Q2230+02	2.15	1.86440	20.85 ± 0.08 (3)	< 12.56	...	< 18.55	< 0.92	...	< 1.01	-0.66 ± 0.09	Zn
J2241+1225	2.63	2.41800	21.15 ± 0.15 (4)	< 12.01	14.94 ± 0.04	< 17.98	< 0.07	-1.36 ± 0.16	< 0.14	-1.36 ± 0.16	S
J2340-0053	2.09	2.05452	20.35 ± 0.15 (4)	< 11.60	14.95 ± 0.004	< 17.56	< 0.46	-0.55 ± 0.15	< 0.52	-0.55 ± 0.15	S
Q2342+34	2.92	2.90899	21.10 ± 0.10 (8)	< 11.96	15.17 ± 0.01	< 17.96	< 0.07	-1.08 ± 0.10	< 0.17	-1.08 ± 0.10	S

HI REFERENCES – (1) Herbert-Fort et al. (2006); (2) Kaplan et al. (2010); (3) Pettini et al. (1994); (4) Prochaska & Wolfe (2009); (5) Kanekar et al. (2009); (6) This paper; (7) Jorgenson et al. (2006); (8) Prochaska et al. (2003a);

Table 3. Wavelengths and Oscillator Strengths of Transitions

Element	Wavelength (Å)	f
SII	1250.584	$5.453 \cdot 10^{-3}$
SII	1253.811	$1.088 \cdot 10^{-2}$
SII	1259.519	$1.624 \cdot 10^{-2}$
OI	1355.598	$1.248 \cdot 10^{-6}$
BII	1362.461	$9.870 \cdot 10^{-1}$

REFERENCE – Morton (2003)

Table 4. Solar abundances

Element	$\log N(X/H)_{\odot} + 12$	Source
B	2.79 ± 0.04^a	Meteoritic
C	8.43 ± 0.05	Photospheric
N	7.83 ± 0.05	Photospheric
O	8.69 ± 0.05	Photospheric
S	7.15 ± 0.02	Meteoritic

REFERENCE – Asplund et al. (2009)

^a The measured solar abundance of boron by Asplund et al. (2009) is higher by ~ 0.3 dex relative to the local ISM and B-type stars that have been used in previous works such as Venn et al. (2002), see also the discussion in Cunha et al. (1997). The impact of the uncertainty in the solar boron abundance is discussed in Section 4.

3 ABUNDANCE DETERMINATION

All metal column densities were obtained using the apparent optical depth method (AODM) outlined by Savage & Sembach (1991). The limits for the optical depth integrations were chosen to contain the absorption profile common for several non-contaminated lines. These limits are shown by the vertical dotted lines in Figures 3, 5, and 7 (although these have been adjusted from their fiducial values in cases of suspected contamination, which we discuss on a case by case basis below). The errors quoted in Table 2 were determined from the photon noise. Continuum errors are typically neglected for strong transition lines as the error is dominated by photon noise. However for the weak detections presented in Section 3.1; continuum fitting errors may play a role in the abundance determination and are further discussed on a case by case basis in Section 3.2.

For the majority of the absorbers in our sample, HI column densities have been previously determined either directly from the SDSS spectra (10 DLAs, Prochaska & Wolfe 2009), follow-up spectroscopy obtained with either Keck II/ESI (3 DLAs, Herbert-Fort et al. 2006) or MMT/BCS (4 DLAs, Kaplan et al. 2010), or were adopted from previous studies (5 DLAs). For the remaining two DLAs, we have determined the $N(\text{HI})$ directly from the HIRES spectrum. HI column densities were determined by fitting a fully damped Voigt profile to the $\text{Ly}\alpha$ transition using a function with the XIDL software. Six DLAs have no measured $N(\text{HI})$ currently available; these are lower redshift DLAs for which neither the original SDSS spectrum nor the new HIRES data cover the $\text{Ly}\alpha$ transition. The systems without an $N(\text{HI})$ measurement are still included in our sample, since a measurement of the B/S or B/O can still help us to constrain production mechanisms.

To estimate 3σ upper limits in the case of non-detections, we took the value of the full width at half maximum (FWHM) of the most prominent feature in the absorption profile of a strong transition. This feature should correspond to the most easily detected absorption of any element in the DLA. From the S/N ratio of the spectrum at the location of the absorption line (see Table 1³), the rest frame equivalent width (W ; at $n\sigma$ significance) of a line at redshift z is calculated from

$$W = \frac{n \cdot FWHM}{S/N \cdot (1+z)}, \quad (1)$$

From equation 1, the column density of a species with rest wavelength λ_0 and oscillator strength f is calculated from

$$N = \frac{\pi e^2}{m_e c^2} \frac{W}{f \lambda_0^2}. \quad (2)$$

All wavelengths, oscillator strengths (Morton 2003), and solar values (Asplund et al. 2009) adopted are listed in Tables 3 and 4, respectively. The measured column densities and derived upper limits are presented in Table 2, along with the quasar emission redshift (z_{em}), DLA absorption redshift (z_{abs}), and HI column densities of the DLAs. All 3σ upper limits presented are only obtained for the spectra where little or no contamination is present using the S/N near the absorption. Otherwise, no upper limit was obtained despite S/N being reported for all DLAs near the line in Table 1.

In this study, we focus solely on the abundances of B, O, and S. We assume that the gas phase abundances that we have measured are representative of the total elemental abundance in the DLA. Oxygen and sulphur are indeed non-refractory and little depleted onto dust grains (Savage & Sembach 1996). Although boron is depleted in dense Galactic disk clouds (Howk et al. 2000), sight-lines through low density gas should yield a robust estimate of the boron abundance (Ritchey et al. 2011). The abundance pattern of DLAs (Pettini et al. 2000), typically low molecular content (Ledoux et al. 2003) and high spin temperature (Ellison et al. 2012) indicate that most DLA sight-lines do not intersect cold, high density clouds. Hence the boron abundances measured in these systems should not be greatly affected by depletion. However, due to the generally higher metallicities of the MSDLAs in our sample, we may be probing higher density sight-lines which may have enhanced dust depletion. We also assume that the measured ionization state for each element is the dominant one and that no ionization corrections are necessary. We discuss explicitly the effect of possible depletion and ionization effects on our conclusions in Section 4.

3.1 Possible Detections

Three of the DLAs in our sample have visibly significant absorption features at the expected wavelength of BII λ 1362. The profiles from each are discussed below, including possible sources of blending and contamination. Figures 2, 4, and

³ The blank S/N ratio entry represents no coverage in the spectrum and is included for completeness. DLAs classified as MSDLAs (based on the silicon and zinc abundances from Berg et al., in prep.) are flagged in the final column.

6 show the absorption profiles for several different species; whereas Figures 3, 5, and 7 zoom in and show the profiles for both boron and oxygen. For comparison the scaled profiles of moderately strong lines are shown for visual guidance of the general shape of absorption profiles for these DLAs⁴.

3.1.1 J0058+0115

Figure 2 displays the absorption features for various transition lines in J0058+0115, whereas Figure 3 shows an absorption feature at the expected wavelength of BII λ 1362 and OI λ 1355. The scaled nickel line is overplotted in Figure 3 for comparison. The shape of the boron absorption is in very good agreement with that of the Ni II λ 1741 line, hence we report a possible detection of boron for the first time in this DLA, where the measured equivalent width is 3.55σ significant⁵. However, it is not feasible to rule out the possibility that this feature is actually a weak Ly α line. The OI λ 1355 line is completely blended with the Ly α forest and we therefore do not report a limit.

3.1.2 FJ0812+3208

Boron was detected in the FJ0812+3208 sight-line at a redshift of $z = 2.626$ by Prochaska et al. (2003b) with a column density $\log N(\text{B}) = 11.43$. The data presented here for this sight-line have been improved from that presented in Prochaska et al. (2003b) by the addition of ~ 10 hours of HIRES data (Jorgenson et al. 2009). Both the BII λ 1362 and OI λ 1355 lines are shown in Figure 5, with scaled CrII λ 2066 shown for comparison. It can be seen that the CrII line has two components: the stronger one centred at $v \sim 0$ km s⁻¹ and a weaker component at ~ -40 km s⁻¹. The CrII profile is used to define the velocity range over which we integrate the optical depth in both OI and BII (vertical dotted lines). The BII λ 1362 line is well aligned with CrII λ 2066. We determine a column density $\log(\text{B}/\text{H}) = 11.43 \pm 0.08$ (measured at 3.84σ significance) which is in agreement with the result of Prochaska et al. (2003b). Figure 5 shows that there is an additional BII λ 1362 component at $v \sim -20$ km s⁻¹ (bounded by the solid vertical green lines) that is not seen in CrII. We have excluded it in the abundance determination. The additional absorption at $v \sim +40$ km s⁻¹ is unrelated absorption and has been excluded from the analysis. The oxygen profile is detected only in the strongest component at $v \sim 0$ km s⁻¹, but not the weaker component seen in other lines at $v \sim -40$ km s⁻¹ (see Figure 2). Given the S/N, we might have expected a detection (albeit weak) of the $v \sim -40$ km s⁻¹ component, if the column densities of the two components have the same relative ratio in oxygen as sulphur. We must therefore consider the possibility

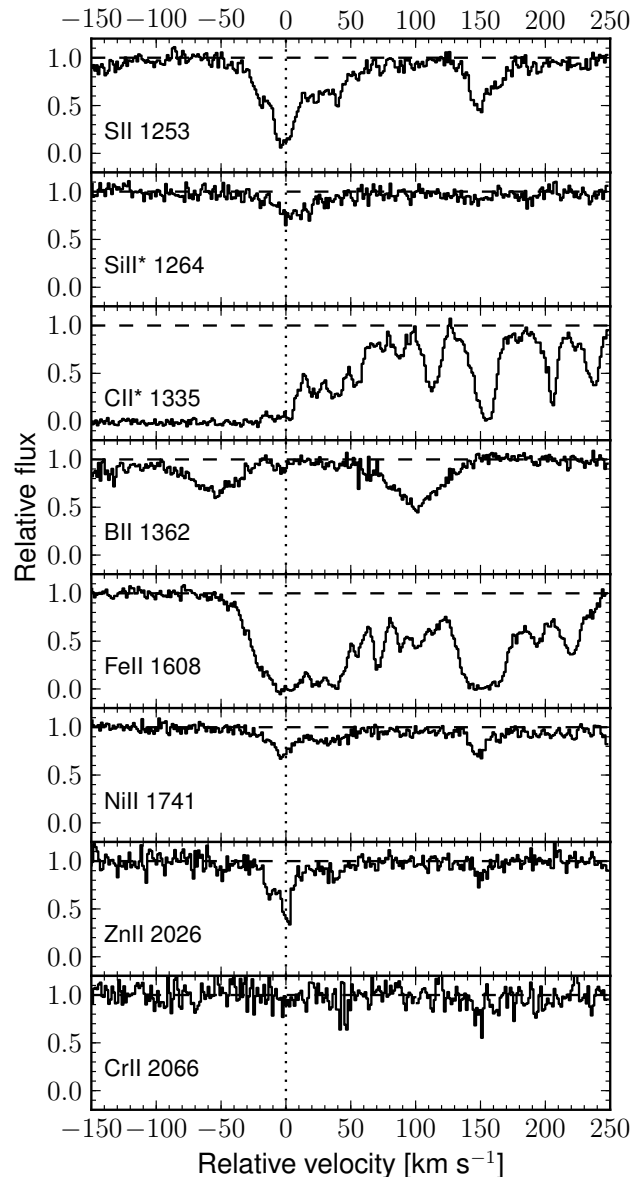


Figure 2. Absorption profiles for various singly ionized species in J0058+0115. From panel to panel, it is apparent that the absorption profiles for all the species (other than CII*) traces out an identical shape for various absorption strengths.

⁴ The scaling is done by matching the area integrated within the AODM bounds for the reference metal line profile to the area determined for boron or oxygen.

⁵ The significance is calculated by combining Equations 1 and 2, then solving for the number of sigma (n) needed to obtain the derived AODM abundance. The FWHM was measured from a prominent absorption component of a strong metal line in the spectrum, and is equivalent to the value used in the calculation for the upper limits.

that the oxygen detection may be contaminated by a different species. Indeed, if the absorption was entirely due to OI, it would yield a $[\text{S}/\text{O}] = -0.67$, which is a surprising discrepancy from the solar value. However, we note that in Prochaska et al. (2003b) $[\text{S}/\text{O}]$ is determined to be $[\text{S}/\text{O}] = -0.33$ which is closer to the relative abundance in nearby disk stars (e.g. Reddy et al. 2003, see Section 4.1). This discrepancy with Prochaska et al. (2003b) is due to both a lower $N(\text{SII})$ and a higher $N(\text{OI})$ in our study. To be con-

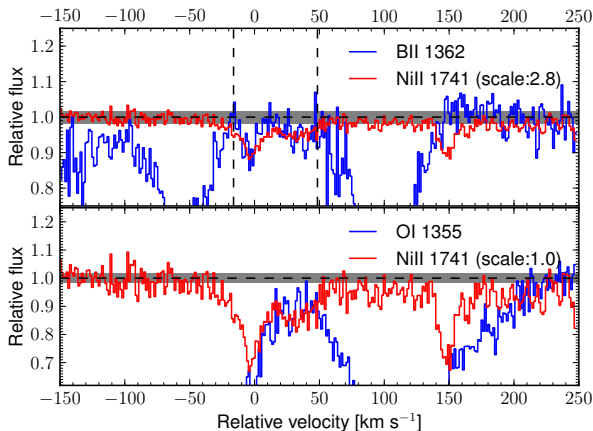


Figure 3. The absorption profile of BII λ 1362 (top, blue), OI λ 1355 (bottom, blue) and SII λ 1250 (red) for J0058+0115. The black horizontal dashed line indicates the continuum, and the black vertical dotted lines are the bounds for the apparent optical depth integration for the species in blue. The nickel profile is scaled down to match the intensity of the boron and oxygen lines by matching the areas within the AODM bounds of the absorption. Oxygen is not detected in this DLA as it is blended within the Ly α forest. Overall, the scaled profile matches that of boron absorption. The grey regions mark where the continuum has been over and underestimated for determining errors in the continuum (see Section 3.2).

servative and because we have a robust detection of sulphur for our analysis; we report oxygen as an upper limit from the equivalent width of the detected absorption feature in recognition of possible contamination.

3.1.3 J1417+4132

J1417+4132 contains a possible detection of boron (see Figure 7) that we report here for the first time. The scaled ZnII λ 2026 line is shown for comparison. The detection is challenging in this case because of the broad, shallow nature of the profile; but there is a clear drop below the continuum over the same velocity range where the boron profile would lie for both OI and BII. However, the feature is broad and shallow, with a total equivalent width significant to 2.97σ , making it a very tentative detection. Despite being nearly 3σ , we adopt the column density as an upper limit due to the challenging nature of the detection. However, a discussion on how the continuum errors may affect the yields of both boron and oxygen is furthered in Section 3.2 for completeness. Unfortunately, all of the SII lines are saturated or severely blended, so we can only determine a lower limit for N(SII).

3.2 Continuum errors

Due to the weakness of the putative boron features, continuum errors may play a role for the three DLAs discussed above. To check how much the continuum placement may affect our results, we artificially placed the continuum at higher and lower values to estimate the difference in column

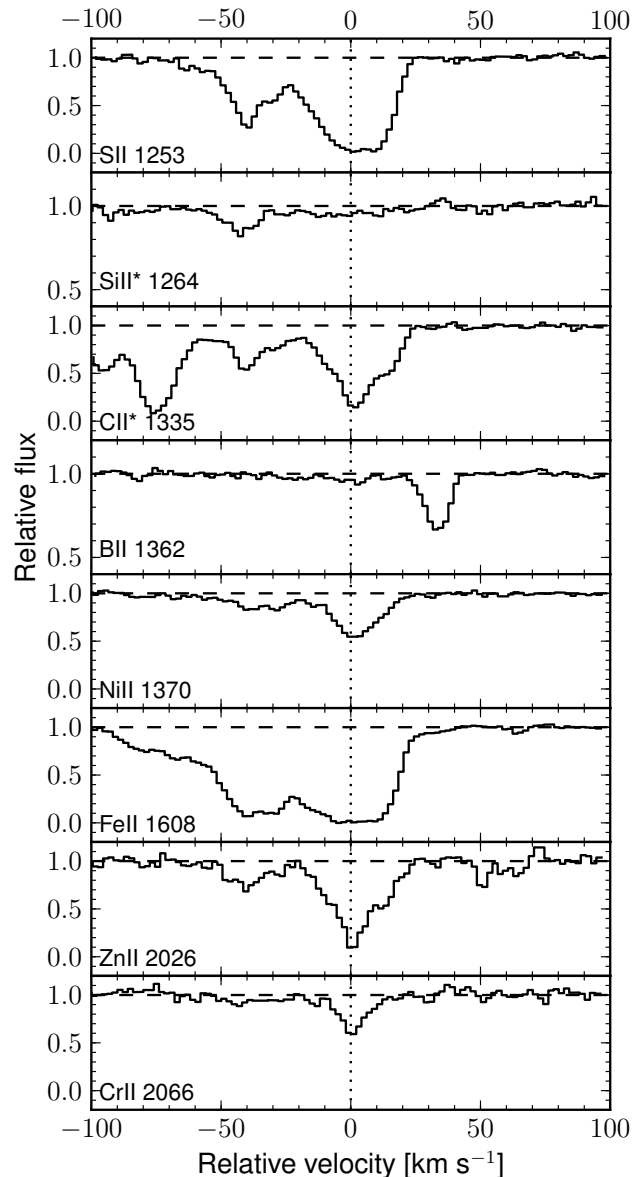


Figure 4. Similar to Figure 2, the same absorption profile is seen for all singly ionized species detected in FJ0812+3208.

density resulting from bad continuum fitting. This is represented by the top and bottom edges of the grayed regions in Figures 3, 5, and 7. These offsets correspond to 40% of the inverse of the S/N of the spectrum near the absorption. The resulting differences in the column densities ($\Delta\log N$) for the associated continuum offsets are shown in Table 5 for both boron and oxygen. In general, the change in column density for both oxygen and boron (< 0.18 dex) is about the same magnitude or smaller than the typical error in the hydrogen column density (0.15–0.25 dex; see Table 2). Specifically, for J1417+4132 (where $\Delta\log N(B)$ is ~ 0.17 dex) the difference

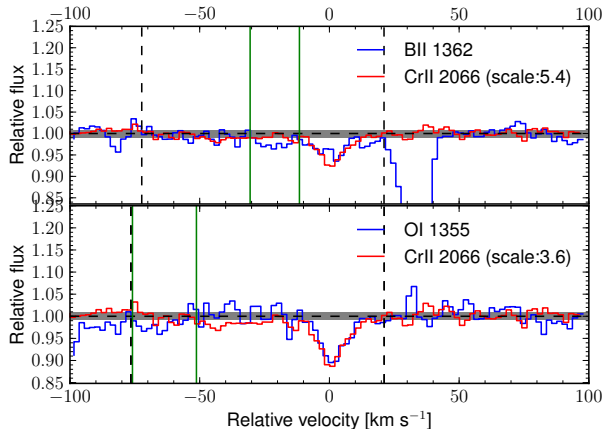


Figure 5. The absorption profile of boron and oxygen for FJ0812+32 following the notation in Figure 3. Extra components that are not present in the chromium profile are bounded by the solid green vertical lines and are not included in the abundance determination. Boron appears to be blended by a feature at $v \sim -20$ km s $^{-1}$, which we have removed from the abundance determination. The oxygen absorption at ~ -40 km s $^{-1}$ does not appear, despite the strength of the component at ~ 0 km s $^{-1}$ and high S/N. See Section 3.1.2 for a discussion of possible contamination of the oxygen line. The grey regions mark where the continuum has been over and underestimated for determining errors in the continuum (see Section 3.2).

is small relative to the overall error budget in [B/H] (0.26 dex) which is primarily dominated by the uncertainty in the hydrogen column (0.25 dex). However the change in column density for boron in both J0058+0115 and FJ0812+3208 is of the same order as the hydrogen column error. The uncertainty in the total error budgets in [O/H] and [B/H] (σ_O and σ_B ; respectively) have been recalculated from Table 2 to include this continuum error and are shown in Table 5. Including the continuum fitting error in the total error budget results in at most a 0.07 dex change, which is relatively small. Based on these results, we conclude that continuum errors do not have a significant contribution in any of these three DLAs.

4 DISCUSSION

4.1 Sulphur-oxygen relation

In order to overcome the difficulties of determining oxygen abundances in stars⁶ and DLAs, we investigate in this work the possibility of using sulphur as an alternative alpha-capture reference element. The comparison of boron with sulphur in the DLAs and stellar data therefore hinges on whether the sulphur abundance intrinsically tracks oxygen in stars. Other than stars containing boron, the stellar literature sources were selected on the basis of what lines and

⁶ Although the comparison with the ISM is more realistic; we include stars as well since we are motivated by determining the nucleosynthetic origin of boron. Previous studies of stars and the ISM provide this information, hence both are included.

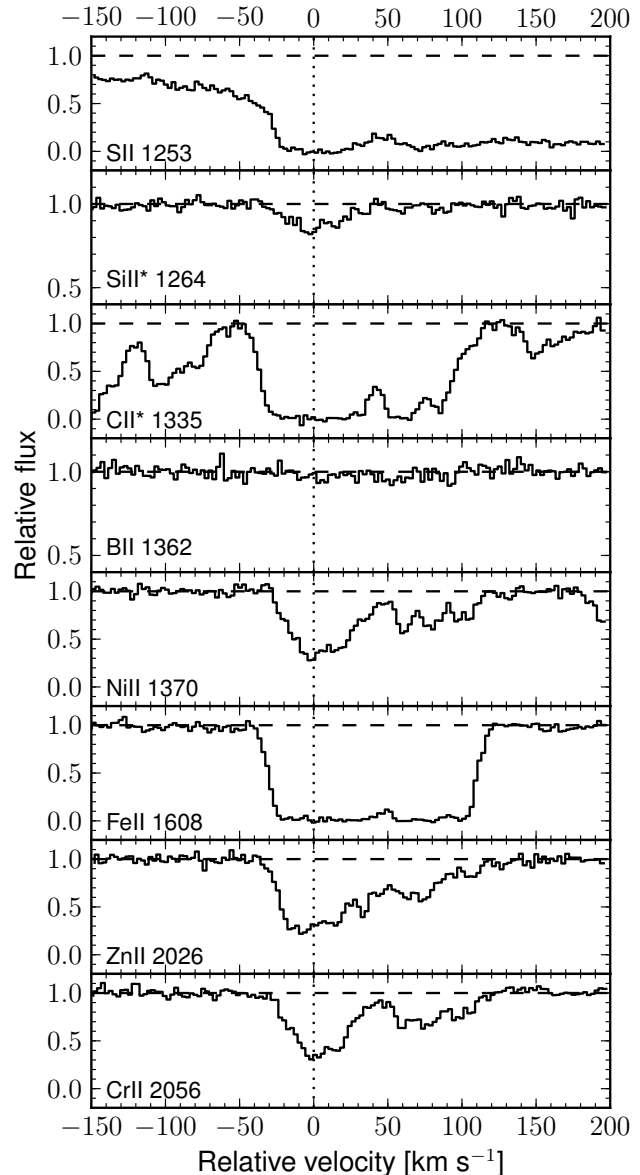


Figure 6. Absorption profiles for various species in J1417+4132. Identical absorption profiles are seen for all singly ionized species (other than SII; which is lost by broad absorption). Again, we note that there seems to be absorption at the Si II* $\lambda\lambda$ 1264.

corrections were used in attempts to homogenize the sample and remove systematic errors (see Table 6⁷). For oxygen, we only selected literature samples that used [O I], UV OH lines with proper continuum placement, or the OI triplet with non-LTE corrections. Following the analysis done by Caffau et al. (2005), sulphur studies that used the S I mul-

⁷ Abundances have been converted to the Asplund et al. (2009) scale.

Table 5. Continuum errors

QSO	Continuum offset	$\Delta\log\text{N}(\text{B})^a$	$\Delta\log\text{N}(\text{O})^a$	$\sigma_{B_{orig}}^b$	$\sigma_{O_{orig}}^b$	$\sigma_{B_{new}}^c$	$\sigma_{O_{new}}^c$
J0058+0115	± 0.013	± 0.14	...	± 0.16	...	± 0.21	...
FJ0812+3208	± 0.007	± 0.18	...	± 0.17	...	± 0.24	...
J1417+4132	± 0.014	$(\pm 0.17)^d$	± 0.15	(± 0.26)	± 0.26	(± 0.31)	± 0.30

^a The error in the column density resulting from offsetting the continuum.

^b The error budget in the abundance $[\text{X}/\text{H}]$ from the AODM calculation (Table 2).

^c The total error budget in the abundance $[\text{X}/\text{H}]$ including the error from continuum placement.

^d The errors in parentheses represent the derived AODM errors from assuming the detection is real.

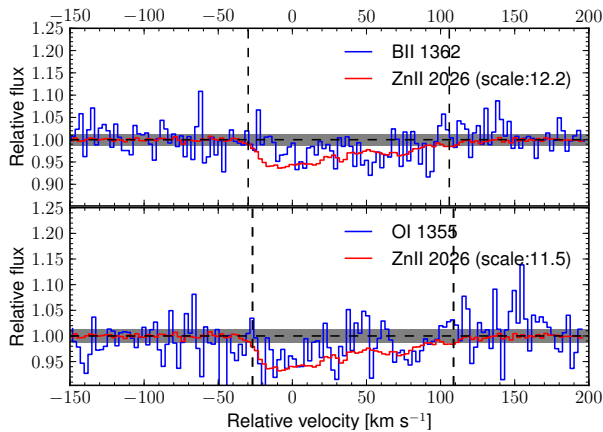


Figure 7. The absorption profiles of boron, oxygen and zinc for J1417+4132 following the same notation as in Figure 5. The grey regions mark where the continuum has been over and underestimated for determining errors in the continuum (see Section 3.2). The absorption is only significant to 2.97σ , so it is treated as an upper limit.

triplet 1 (with non-LTE corrections), 6, and 8 for abundance determinations were selected. DLAs not present in our sample which contained both oxygen and sulphur abundances are included as well solely for comparison.

Figure 8 shows the relation between $[\text{S}/\text{O}]$ and $[\text{O}/\text{H}]$ for the literature sample used. DLAs are not included in determining the mean offset as they are only shown for interest. Although the scatter about the mean appears substantial, most of the stellar data are consistent within 1.5σ of the mean. Having a constant offset in stars suggests that the interchange of oxygen and sulphur is valid, and should not change the slope of the best fit line between B/O and B/S. Due to the variety in non-LTE corrections, model atmospheres, and choice of lines; a more homogeneous dataset of oxygen and sulphur in stars should tighten the relation.

4.2 Boron-oxygen relation

In Figure 9 we present our main scientific results, the comparison of DLA and Galactic boron abundances plotted as a function of oxygen (left) and sulphur (right). Both panels contain the primary and secondary lines (of slopes $m = 1$ and $m = 2$, respectively) and the best fit lines we have derived from a linear least squares fit:

$$[B/H] = (1.48 \pm 0.059)[O/H] - (0.26 \pm 0.110) \quad (3)$$

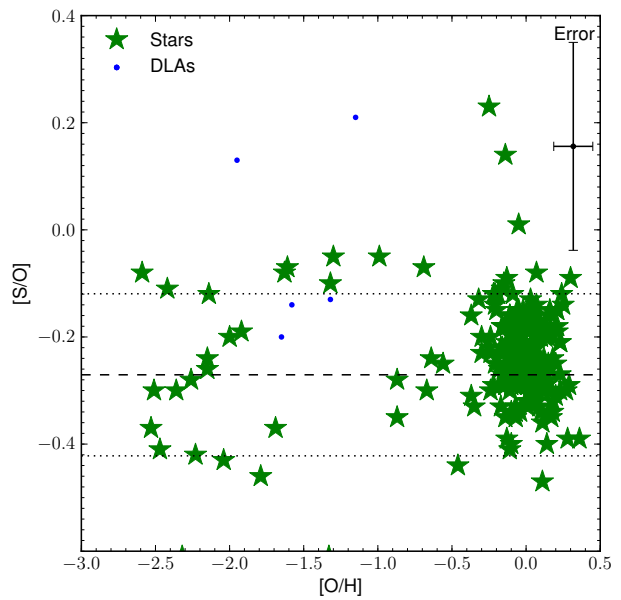


Figure 8. $[\text{S}/\text{O}]$ is plotted as a function of $[\text{O}/\text{H}]$ for stellar data to determine whether these two element track each other in stars. The data plotted includes the entire literature compilation presented in Table 6, including both stars and DLAs. The dashed line is the mean value of $[\text{S}/\text{O}] = -0.27 \pm 0.15$ (with dotted lines as 1σ errors) of the plotted data. The error bar in the top right shows the typical uncertainty in the stellar abundances.

and

$$[B/H] = (1.40 \pm 0.117)[S/H] - (0.04 \pm 0.121). \quad (4)$$

These best fit lines only include all detections in the Milky Way from Smith et al. (2001) and Tan et al. (2010), as well as the solar value (Asplund et al. 2009)⁸. We also included in the fit B stars that appeared not to be affected by rotational mixing⁹ and ISM sight-lines that contained warm

⁸ As the solar point is included, we do not force the primary, secondary, and best-fit lines through it.

⁹ Based on stars with $\log(\text{N}/\text{H}) < -4.2$; $\log(\text{B}/\text{H}) > -10.0$ from (Venn et al. 2002). Note that there still may be boron depletion (Mendel et al. 2006) as boron depletion occurs before nitrogen enrichment.

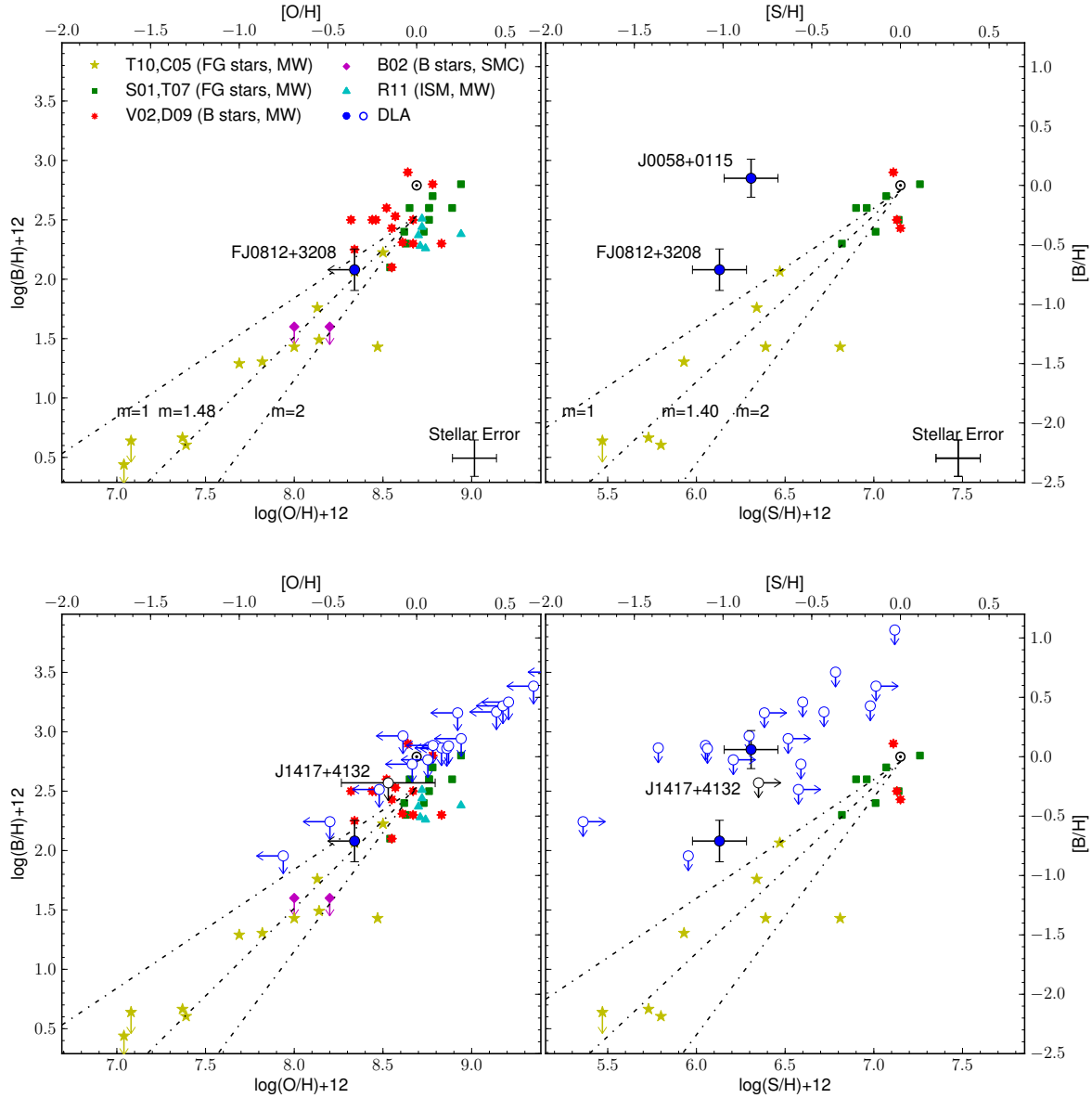


Figure 9. B/H is plotted as a function of O/H (left panels) and S/H (right panels). The stellar boron data is from Smith et al. (2001) (S01), Tan et al. (2010) (T10), Venn et al. (2002) (V02), Brooks et al. (2002) (B02). The sulphur abundances for the Galactic data were adopted from Caffau et al. (2005) (C05), Takeda (2007) (T07), and Dafon et al. (2009) (D09). Open circles are used for any boron upper limits in DLAs, whereas the filled circles represent possible detections. The top set of panels only show the data of the two identified DLAs (J0058+0112 and FJ0812+3208), whereas the bottom panels include all upper limits as well. Typical errors in the stellar data are shown in the bottom right of the top panels. The solar (Asplund et al. 2009) scale is included along the top and right axes in both panels. The best fit equations are: $[B/H] = (1.48 \pm 0.059)[O/H] - (0.26 \pm 0.110)$ (left); $[B/H] = (1.40 \pm 0.117)[S/H] - (0.04 \pm 0.121)$ (right). As the Asplund et al. (2009) values are included in the fit, we do not force the lines to pass through the origin.

gas (Ritchey et al. 2011)¹⁰. Both primary and secondary

lines are forced to go through the origin of the best fit. The

¹⁰ The Ritchey et al. (2011) sample contains a compilation 56 sight-lines. Only the 6 lowest density sight-lines from the sample

were chosen for our dataset as they are relatively unaffected by dust depletion.

B-O relation agrees with the best fit equations presented in Smith et al. (2001) and Ritchey et al. (2011) (which have $m = 1.39 \pm 0.08, 1.5 \pm 0.1$; respectively).

For the first time, we can now place high redshift data points on the boron abundance plot. The traditional presentation of oxygen and boron abundances is shown in the left panels of Figure 9. Note that, for convenience, axes are labeled for both B/H and [B/H] (similarly for oxygen). Only the potential detections are plotted in the top panels of Figure 9, whereas all data (including the limits) are shown in the bottom panels. The DLA boron upper limits are above the primary ($m = 1$) line and therefore do not provide useful constraints on boron production in the DLAs. Moreover, we have no further measurements of O/H, so the DLA points are limits in both quantities. Note that these limits cluster parallel to the $m = 1$ line because the BII λ 1362 and OI λ 1355 lines are so close in wavelength that their S/N ratios are essentially identical. In combination with the same assumed FWHM of the strongest feature (see Section 3) and similar $f \cdot (\frac{X}{H})_{\odot}$, Equation 2 implies nearly equal abundances limits of boron and oxygen for each system.

Relative to oxygen, FJ0812+3208 is still consistent with the primary line. However, we have conservatively reported the oxygen abundance in FJ0812+3208 as an upper limit.

Turning now to the B-S abundances which are shown in the right panels of Figure 9. In addition to circumventing the problem of uncertain stellar O/H abundances, it can be seen that sulphur has the added advantage of being measurable in many of the DLAs. Nonetheless, the boron non-detections all lie above the primary line, so the production of boron is *not constrained*. However, both J0058+0115 and FJ0812+3208, which have robust detections in both B and S are above the primary line, with the inclusion of the continuum errors mentioned in Section 3.2.

The data presented here reveal the *possibility* of super-primary boron abundances in two DLAs (indeed, the only two where boron is tentatively detected) at high z . Although these two DLAs are unlikely to be representative of the DLA population, their high N(HI) and relatively high metallicities are unusual but make them ideal for a conceptual study of boron. We now consider possible corrections that are required to the abundances that we have determined, and the impact on our interpretation of the data.

- *Dust depletion.* Sulphur and oxygen are not expected to have appreciable depletion on to dust, but boron is mildly refractory (Howk et al. 2000). Dust depletion would raise the boron abundance above the gas phase value we have measured, pushing the DLA data points upwards, and hence even further above the primary line. Hence, dust can not explain the possible super-primary boron abundances in the two DLAs.

- *Ionization effects.* Ionization has little effect on the oxygen and sulphur abundances. Corrections for ionization have been modeled extensively for DLAs in both hard and soft ionizing radiation fields (e.g. Vladilo et al. 2001; Rix et al. 2007). Due to charge exchange reactions, the ionization correction for oxygen is negligible. Although photoionization by a stellar radiation field could lead to an under-estimate of the [S/H] from SII, and push the DLA data points closer to the $m = 1$ line, at the hydrogen column density of FJ0812+3208 the correction is less than 0.05 dex (Vladilo et al. 2001). Al-

though boron has not been included in previous ionization models, the high N(HI) in FJ0812+3208 ($\log N(\text{HI})=21.35$) means that it is unlikely that a ~ 0.5 dex correction is required, so we also rule out ionization effects as the reason for high boron abundances in these two DLAs.

- *Blending/contamination.* We can not rule out that the main features we have identified as boron are in fact due to contaminating Ly α forest (or other species) lines, (e.g. J0058+0115). We also consider the presence of other weak features within the velocity window over which the integrated optical depth has been calculated. For example, the absorption profiles for FJ0812+3208 in Figure 5 do show signs of other absorption features within the velocity window for both oxygen and boron.

- *Misplaced continuum.* For very weak lines, the continuum placement can be critical. Each spectrum has been visually inspected to see if the continuum fit seems reasonable and manual adjustments made if necessary. Overall, the continuum appears to be well-defined. Section 3.2 demonstrates that continuum placements can account for a difference in the boron column density by as much as ~ 0.18 dex in the most extreme case (FJ0812+3208). These continuum offsets can add up to 0.07 dex to the total error budget, thus having a minimal effect to the overall observations.

After excluding corrections due to dust, ionization, continuum errors and additional components as possible causes for potential super-primary boron abundances, we now consider the possible physical mechanisms for high boron abundances. One intriguing possibility is an enhanced cosmic ray flux that would result in a higher spallation rate of CNO targets to produce the excess boron. Assuming that the cosmic ray flux scales linearly with the boron abundance; J0058+0115 and FJ0812+3208 would have a cosmic ray flux of $\sim 8\times$ and $\sim 2\times$ (respectively) the expected flux for primary production of boron in the Milky Way. A high cosmic ray flux could be associated with a line of sight that intersects gas near a supernova remnant, star forming region, or young cluster (for a list of observed sight-lines see Ritchey et al. 2011). Such sight-lines through enhanced star forming environments might explain the high N(HI) and high metallicity of the two DLAs with boron detections in our sample. Prochaska et al. (2003b) also note the rare detection of the excited SiII* in FJ0812+3208 (see Figure 4), a species that can be used in conjunction with CII* to constrain the gas temperature (Howk et al. 2005)¹¹. Remarkably, J1417+4132 also has a detection of SiII*. To date, SiII* has only been seen in one other DLA (Kulkarni et al. 2012).

As discussed in the Introduction, carbon is also a potential spallation target. Typically it is disregarded during cosmic ray spallation as it is less abundant than oxygen. For example, in the Milky Way, there are typically 6 oxygen nuclei for every carbon, $\log N(\text{C})/N(\text{O}) \sim -0.8$ (Akerman et al. 2004; Fabbian et al. 2009), for $-2.5 \leq [\text{O}/\text{H}] \leq -0.5$. This is not true at $[\text{O}/\text{H}] \sim -3$ and $[\text{O}/\text{H}] \sim 0$, where $[\text{C}/\text{O}]$ becomes solar ($\log N(\text{C})/N(\text{O}) \sim -0.3$; 2 oxygen nuclei for every carbon). For our detections in Figure 9, we would expect carbon spallation to contribute to boron production slightly.

¹¹ This calculation is beyond the scope of the paper. For the interested reader, see Wolfe et al. (2003).

Assuming that there is one carbon atom for every two oxygen as an upper limit, we would expect a shift of ~ 0.18 dex to the right in Figure 9 to account for the extra spallation target (as there are $1.5\times$ as many targets). However, this is an overestimate as there are probably more than two oxygen per carbon atom (as $[O/H] < 0$) so both detected points would still lie above the primary line. If a galaxy were enriched in carbon relative to oxygen, it is plausible that the boron production could exceed that expected from primary oxygen-only spallation. Due to the difficulty of measuring carbon in DLAs (C II $\lambda 1334$ is generally saturated whereas C II $\lambda 2325$ is too weak to be detected), it is difficult to test whether our DLAs are indeed carbon rich. However studies of carbon in DLAs (Pettini et al. 2008; Penprase et al. 2010; Cooke et al. 2011) follow a similar pattern in the $[C/O]$ to the Milky Way at low metallicities.

The results presented in this study demonstrate the possibility of boron detection in DLAs, but also clearly illustrate its challenges. In most of the sight-lines of our study, despite the selection of DLAs with strong metal lines, the upper limits are not deep enough to constrain boron production. In order to assess future prospects for more boron detections, we show in Figure 10 the required S/N ratios per pixel at the BII $\lambda 1362$ line as a function of the sulphur abundance based on Equations 1 and 2 for three different hydrogen column densities, assuming the corresponding FWHM for a b -value¹² of 10 km s^{-1} . Figure 10 suggests that for a DLA with a reasonably high $\log N(\text{HI})=21$ and high metallicity ($[S/H] > -0.6$), boron that has been synthesized via a primary process could be detected in a spectrum with $S/N \sim 50$, which remains moderately demanding on current 8–10 metre class telescopes. Assuming that the exposure time varies as the square of the S/N ratio, our sample of DLAs with upper limits of boron would need exposure times of at least an order of magnitude greater than those listed in Table 1. The detection of high redshift boron would be an excellent science case for the next generation of large optical telescopes with blue optimized echelle spectrographs, such as the High-Resolution Optical Spectrometer for the Thirty Meter Telescope.

5 CONCLUSION

We have presented 2 detections of boron at $> 3\sigma$, 21 upper limits, and one further DLA in which the absorption is suggestive of a boron detection, but formally only significant at 2.97 sigma. The results hint at an excess of boron relative to predictions from primary production in the two cases where we have positive detections; albeit they are still consistent with the primary production mechanism. Although they are presented, it is unclear whether detections are truly real. We rule out that the potential super-primary boron abundances are due to dust or ionization effects and discuss possible physical reasons for the overabundance. Higher boron abundances might be due to higher cosmic ray fluxes in these two DLAs, relative to the Galactic value. This study also has shown that sulphur can be used in place of oxygen for

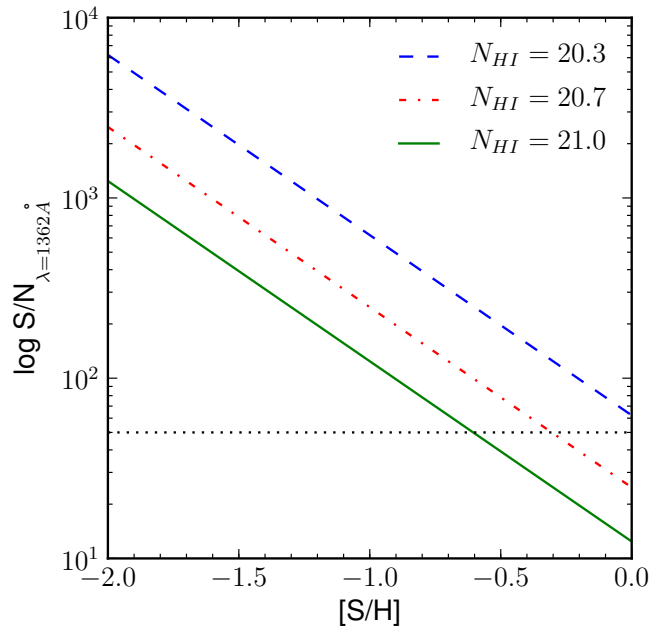


Figure 10. The S/N ratio (per pixel) required to observe primary boron is plotted from Equations 2 and 1 for the range in sulphur values for a fixed redshift of $z_{abs} = 2$. A FWHM corresponding to a $b = 10 \text{ km s}^{-1}$ is assumed as it represents the minimum detectable line width by HIRES. The black dotted line at S/N of 50 is drawn to represent an achievable S/N ratio.

studies of boron. This is useful as oxygen abundances are often unreliable and difficult to obtain in the Milky Way stars, ISM, and DLAs. Figure 10 demonstrates that for high S/N ratios of ~ 50 , DLAs with high metallicities ($[S/H] > -0.6$ dex) and high HI columns ($\log N(\text{HI}) \sim 21$) are needed to test whether DLAs do in fact exhibit higher boron abundances relative to primary production.

ACKNOWLEDGMENTS

We would like to thank the anonymous referee for their useful comments to ensure the clarity of this work. We gratefully acknowledge the efforts of M. Neeleman in reducing some of the spectra presented here and for his helpful comments on this manuscript. JXP acknowledges support from NSF grant AST-1109447. The authors wish to recognize and acknowledge the very significant cultural role and reverence that the summit of Mauna Kea has always had within the indigenous Hawaiian community. We are most fortunate to have the opportunity to conduct observations from this mountain.

REFERENCES

- Abdo A. A. et al., 2010, A&A, 523, A46
- Akerman C. J., Carigi L., Nissen P. E., Pettini M., Asplund M., 2004, A&A, 414, 931
- Asplund M., Grevesse N., Sauval A. J., Scott P., 2009, ARA&A, 47, 481
- Boesgaard A. M., Deliyannis C. P., King J. R., Ryan S. G., Vogt S. S., Beers T. C., 1999a, AJ, 117, 1549

¹² The b -value is related to the FWHM by $FWHM = 2\sqrt{\ln 2}b$

- Boesgaard A. M., King J. R., Deliyannis C. P., Vogt S. S., 1999b, *AJ*, 117, 492
- Brooks A. M., Venn K. A., Lambert D. L., Lemke M., Cunha K., Smith V. V., 2002, *ApJ*, 573, 584
- Caffau E., Bonifacio P., Faraggiana R., François P., Gratton R. G., Barbieri M., 2005, *A&A*, 441, 533
- Carretta E., Gratton R. G., Sneden C., 2000, *A&A*, 356, 238
- Cooke R., Pettini M., Steidel C. C., Rudie G. C., Nissen P. E., 2011, *MNRAS*, 417, 1534
- Cunha K., Lambert D. L., Lemke M., Gies D. R., Roberts L. C., 1997, *ApJ*, 478, 211
- Cunha K., Smith V. V., Boesgaard A. M., Lambert D. L., 2000, *ApJ*, 530, 939
- Dafon S., Cunha K., de la Reza R., Holtzman J., Chiappini C., 2009, *AJ*, 138, 1577
- Dessauges-Zavadsky M., Calura F., Prochaska J. X., D’Odorico S., Matteucci F., 2007, *A&A*, 470, 431
- Duncan D. K., Lambert D. L., Lemke M., 1992, *ApJ*, 401, 584
- Duncan D. K., Primas F., Rebull L. M., Boesgaard A. M., Deliyannis C. P., Hobbs L. M., King J. R., Ryan S. G., 1997, *ApJ*, 488, 338
- Ellison S. L., Kanekar N., Prochaska J. X., Momjian E., Worseck G., 2012, *MNRAS*, 424, 293
- Fabbian D., Nissen P. E., Asplund M., Pettini M., Akerman C., 2009, *A&A*, 500, 1143
- Federman S. R., Sheffer Y., Lambert D. L., Gilliland R. L., 1993, *ApJL*, 413, L51
- Fields B. D., Olive K. A., Vangioni-Flam E., Cassé M., 2000, *ApJ*, 540, 930
- García Lopez R. J., Lambert D. L., Edvardsson B., Gustafsson B., Kiselman D., Rebolo R., 1998, *ApJ*, 500, 241
- Herbert-Fort S., Prochaska J. X., Dessauges-Zavadsky M., Ellison S. L., Howk J. C., Wolfe A. M., Prochter G. E., 2006, *PASP*, 118, 1077
- Howk J. C., Sembach K. R., Savage B. D., 2000, *ApJ*, 543, 278
- Howk J. C., Wolfe A. M., Prochaska J. X., 2005, *ApJL*, 622, L81
- Israelian G., Rebolo R., García López R. J., Bonifacio P., Molaro P., Basri G., Shchukina N., 2001, *ApJ*, 551, 833
- Jorgenson R. A., Wolfe A. M., Prochaska J. X., Carswell R. F., 2009, *ApJ*, 704, 247
- Jorgenson R. A., Wolfe A. M., Prochaska J. X., Lu L., Howk J. C., Cooke J., Gawiser E., Gelino D. M., 2006, *ApJ*, 646, 730
- Jura M., Meyer D. M., Hawkins I., Cardelli J. A., 1996, *ApJ*, 456, 598
- Kanekar N., Smette A., Briggs F. H., Chengalur J. N., 2009, *ApJL*, 705, L40
- Kaplan K. F., Prochaska J. X., Herbert-Fort S., Ellison S. L., Dessauges-Zavadsky M., 2010, *PASP*, 122, 619
- Korn A. J., Becker S. R., Gummertsbach C. A., Wolf B., 2000, *A&A*, 353, 655
- Kraft R. P., Sneden C., Langer G. E., Prosser C. F., 1992, *AJ*, 104, 645
- Kulkarni V. P., Meiring J., Som D., Péroux C., York D. G., Khare P., Lauroesch J. T., 2012, *ApJ*, 749, 176
- Ledoux C., Petitjean P., Srianand R., 2003, *MNRAS*, 346, 209
- Lopez S., Reimers D., D’Odorico S., Prochaska J. X., 2002, *A&A*, 385, 778
- Mendel J. T., Venn K. A., Proffitt C. R., Brooks A. M., Lambert D. L., 2006, *ApJ*, 640, 1039
- Meneguzzi M., York D. G., 1980, *ApJL*, 235, L111
- Morton D. C., 2003, *ApJS*, 149, 205
- Nissen P. E., Akerman C., Asplund M., Fabbian D., Kerber F., Kaufl H. U., Pettini M., 2007, *A&A*, 469, 319
- Nissen P. E., Chen Y. Q., Asplund M., Pettini M., 2004, *A&A*, 415, 993
- Penprase B. E., Prochaska J. X., Sargent W. L. W., Toromartinez I., Beeler D. J., 2010, *ApJ*, 721, 1
- Petitjean P., Ledoux C., Srianand R., 2008, *A&A*, 480, 349
- Pettini M., Ellison S. L., Bergeron J., Petitjean P., 2002, *A&A*, 391, 21
- Pettini M., Ellison S. L., Steidel C. C., Shapley A. E., Bowen D. V., 2000, *ApJ*, 532, 65
- Pettini M., Smith L. J., Hunstead R. W., King D. L., 1994, *ApJ*, 426, 79
- Pettini M., Zych B. J., Steidel C. C., Chaffee F. H., 2008, *MNRAS*, 385, 2011
- Prantzos N., 2012, *A&A*, 542, A67
- Prochaska J. X., Gawiser E., Wolfe A. M., Cooke J., Gelino D., 2003a, *ApJS*, 147, 227
- Prochaska J. X., Howk J. C., Wolfe A. M., 2003b, *Nature*, 423, 57
- Prochaska J. X., Wolfe A. M., 2009, *ApJ*, 696, 1543
- Prochaska J. X., Wolfe A. M., Howk J. C., Gawiser E., Burles S. M., Cooke J., 2007, *ApJS*, 171, 29
- Rafelski M., Wolfe A. M., Prochaska J. X., Neeleman M., Mendez A. J., 2012, *ArXiv e-prints*
- Ramírez I., Meléndez J., Chanamé J., 2012, *ApJ*, 757, 164
- Reddy B. E., Tomkin J., Lambert D. L., Allende Prieto C., 2003, *VizieR Online Data Catalog*, 734, 304
- Reeves H., Fowler W. A., Hoyle F., 1970, *Nature*, 226, 727
- Rich J. A., Boesgaard A. M., 2009, *ApJ*, 701, 1519
- Ritchey A. M., Federman S. R., Sheffer Y., Lambert D. L., 2011, *ApJ*, 728, 70
- Rix S. A., Pettini M., Steidel C. C., Reddy N. A., Adelberger K. L., Erb D. K., Shapley A. E., 2007, *ApJ*, 670, 15
- Salmon S., Montalbán J., Morel T., Miglio A., Dupret M.-A., Noels A., 2012, *MNRAS*, 422, 3460
- Savage B. D., Sembach K. R., 1991, *ApJ*, 379, 245
- Savage B. D., Sembach K. R., 1996, *ARA&A*, 34, 279
- Smith V. V., Cunha K., King J. R., 2001, *AJ*, 122, 370
- Spite M. et al., 2011, *A&A*, 528, A9
- Spite M. et al., 2005, *A&A*, 430, 655
- Sreekumar P. et al., 1993, *Physical Review Letters*, 70, 127
- Srianand R., Petitjean P., Ledoux C., Ferland G., Shaw G., 2005, *MNRAS*, 362, 549
- Takeda Y., 2007, *PASJ*, 59, 335
- Tan K., Shi J., Zhao G., 2010, *ApJ*, 713, 458
- Venn K. A., Brooks A. M., Lambert D. L., Lemke M., Langer N., Lennon D. J., Keenan F. P., 2002, *ApJ*, 565, 571
- Vladilo G., Centurión M., Bonifacio P., Howk J. C., 2001, *ApJ*, 557, 1007
- Wolfe A. M., Gawiser E., Prochaska J. X., 2005, *ARA&A*, 43, 861
- Wolfe A. M., Prochaska J. X., Gawiser E., 2003, *ApJ*, 593, 215

Woosley S. E., Hartmann D. H., Hoffman R. D., Haxton
W. C., 1990, ApJ, 356, 272
Woosley S. E., Weaver T. A., 1995, ApJS, 101, 181

Table 6: Literature boron, oxygen, and sulphur abundances

ID	[O/H]	[S/H]	[B/H]	References
Stars				
HD19994	0.25 ± 0.06	0.11 ± 0.10	0.01 ± 0.20	1,2
HD159332	-0.07 ± 0.06	...	-0.39 ± 0.20	1,2
HD5015	0.07 ± 0.06	-0.01 ± 0.10	-0.29 ± 0.20	1,2
HD216385	0.04 ± 0.06	-0.14 ± 0.10	-0.39 ± 0.20	1,2
HD185395	0.07 ± 0.06	-0.19 ± 0.10	-0.19 ± 0.20	1,2
HD184499	-0.15 ± 0.06	...	-0.69 ± 0.20	1,2
HD210027	-0.04 ± 0.06	...	-0.19 ± 0.20	1,2
HD128167	-0.06 ± 0.06	-0.33 ± 0.10	-0.49 ± 0.20	1,2
HD82328	0.07 ± 0.06	-0.25 ± 0.10	-0.19 ± 0.20	1,2
HD4813	0.09 ± 0.06	-0.08 ± 0.10	-0.09 ± 0.20	1,2
HD28033	0.20 ± 0.06	...	-0.19 ± 0.20	1,2
NGC346-637	-0.69 ± 0.2	...	< -1.19	3
AV304	-0.49 ± 0.2	...	< -1.19	3
HD194598	-0.69 ± 0.10	-0.76 ± 0.15	-1.36 ± 0.14	4,5
HD94028	-0.87 ± 0.10	-1.22 ± 0.15	-1.48 ± 0.16	4,5
BD+23°3130	-1.58 ± 0.10	...	-2.88 ± 0.25	4
HD76932	-0.35 ± 0.10	-0.68 ± 0.15	-0.72 ± 0.14	4,5
HD201891	-0.56 ± 0.10	-0.81 ± 0.15	-1.03 ± 0.15	4,5
HD19445	-1.32 ± 0.10	-1.42 ± 0.15	-2.12 ± 0.19	4,5
HD84937	-1.61 ± 0.10	-1.68 ± 0.15	< -2.15	4,5
BD+26°3578	-1.65 ± 0.10	...	< -2.35	4
HD160617	-1.30 ± 0.10	-1.35 ± 0.15	-2.18 ± 0.20	4,5
HD184499	-0.19 ± 0.10	...	-0.56 ± 0.17	4
HD64090	-1.00 ± 0.10	...	-1.50 ± 0.13	4
BD+03°740	-2.08 ± 0.10	...	< -2.13	4
BD-13°3442	-2.14 ± 0.10	-2.26 ± 0.15	< -2.35	4,5
HD106516	-0.22 ± 0.10	-0.34 ± 0.15	-1.36 ± 0.15	4,5
HD140283	-1.69 ± 0.10	-2.06 ± 0.15	-2.60 ± 0.22	4,5
HD221377	-0.55 ± 0.10	...	-1.30 ± 0.19	4
HD37744	-0.23 ± 0.20	...	-0.29 ± 0.10	6
HD44743	0.09 ± 0.20	...	0.01 ± 0.10	6
HD36959	-0.08 ± 0.20	0.01 ± 0.14	-0.29 ± 0.10	6,7
HD36629	-0.37 ± 0.20	...	-0.29 ± 0.10	6
HD36351	-0.17 ± 0.20	...	-0.19 ± 0.10	6
HD214993	0.14 ± 0.20	...	-0.49 ± 0.10	6
HD216916	-0.08 ± 0.20	...	-0.48 ± 0.10	6
HD35337	-0.14 ± 0.20	...	-0.69 ± 0.10	6
HD37356	-0.25 ± 0.20	-0.02 ± 0.14	-0.29 ± 0.10	6,7
HD35039	-0.35 ± 0.20	0.03 ± 0.15	0.13 ± 0.10	6,7
HD29248	-0.02 ± 0.20	...	-0.29 ± 0.10	6
BD+56°576	-0.35 ± 0.20	...	-0.54 ± 0.10	6
HD34816	-0.02 ± 0.20	...	-0.49 ± 0.10	6
LP815-43	-1.86 ± 0.15	-2.49 ± 0.22	...	8,9
CS22873-055	-2.42 ± 0.25	-2.53 ± 0.10	...	10,11
CS30325-094	-2.53 ± 0.25	-2.90 ± 0.18	...	10,11
HD179626	-0.46 ± 0.03	-0.90 ± 0.22	...	8,12
CS22948-066	-2.20 ± 0.25	-2.83 ± 0.14	...	10,11
G64-12	-2.24 ± 0.15	-3.00 ± 0.22	...	8,9
G18-39	-0.87 ± 0.04	-1.15 ± 0.22	...	8,12
HD148816	-0.24 ± 0.03	-0.44 ± 0.15	...	5,12
CS29518-051	-1.84 ± 0.25	-2.58 ± 0.10	...	10,11
CS22186-025	-2.36 ± 0.25	-2.66 ± 0.10	...	10,11
LP635-14	-2.00 ± 0.12	-2.20 ± 0.22	...	8,9
CS22896-154	-1.70 ± 0.25	-2.52 ± 0.08	...	10,11
HD2796	-1.92 ± 0.25	-2.11 ± 0.10	...	10,11

Continued on next page

Table 6 – continued from previous page

ID	[O/H]	[S/H]	[B/H]	References
G11–44	-1.63 ± 0.15	-1.71 ± 0.22	...	8,9
HD106516	-0.16 ± 0.03	-0.34 ± 0.15	...	5,12
HD76932	-0.37 ± 0.03	-0.68 ± 0.15	...	5,12
CS29491–053	-2.23 ± 0.25	-2.65 ± 0.10	...	10,11
CS22891–209	-2.47 ± 0.25	-2.88 ± 0.15	...	10,11
G53–41	-0.99 ± 0.05	-1.04 ± 0.22	...	8,12
HD194598	-0.67 ± 0.03	-0.97 ± 0.22	...	8,12
LP651–4	-2.04 ± 0.14	-2.47 ± 0.22	...	8,9
CS22966–057	-1.58 ± 0.25	-2.45 ± 0.10	...	10,11
G64–37	-2.32 ± 0.14	-2.93 ± 0.22	...	8,9
BD–13°3442	-2.15 ± 0.15	-2.41 ± 0.22	...	8,9
BD+17°3248	-1.33 ± 0.25	-1.94 ± 0.10	...	10,11
CS31082–001	-2.26 ± 0.25	-2.54 ± 0.10	...	10,11
BD–18°5550	-2.59 ± 0.25	-2.67 ± 0.12	...	10,11
HD122563	-2.15 ± 0.25	-2.39 ± 0.10	...	10,11
HD186478	-1.79 ± 0.25	-2.25 ± 0.08	...	10,11
CS22953–003	-2.04 ± 0.25	-2.68 ± 0.10	...	10,11
HD193901	-0.64 ± 0.03	-0.88 ± 0.22	...	8,12
CS22956–050	-2.16 ± 0.25	-2.91 ± 0.20	...	10,11
CS22892–052	-2.51 ± 0.25	-2.81 ± 0.10	...	10,11
HD9091	-0.04 ± 0.15	-0.32 ± 0.15	...	13
HD20427	-0.12 ± 0.15	-0.39 ± 0.15	...	13
HD112887	0.02 ± 0.15	-0.26 ± 0.15	...	13
HD2663	-0.11 ± 0.15	-0.37 ± 0.15	...	13
HD209858	0.00 ± 0.15	-0.23 ± 0.15	...	13
HD7228	0.13 ± 0.15	-0.07 ± 0.15	...	13
HD157467	0.30 ± 0.15	0.21 ± 0.15	...	13
HD218172	0.07 ± 0.15	-0.15 ± 0.15	...	13
HD133641	-0.06 ± 0.15	-0.34 ± 0.15	...	13
HD210457	0.04 ± 0.15	-0.22 ± 0.15	...	13
HD222155	0.09 ± 0.15	-0.18 ± 0.15	...	13
HD103891	-0.06 ± 0.15	-0.21 ± 0.15	...	13
HD42618	0.02 ± 0.15	-0.15 ± 0.15	...	13
HD80218	0.10 ± 0.15	-0.19 ± 0.15	...	13
HD109303	0.11 ± 0.15	-0.36 ± 0.15	...	13
HD198390	0.02 ± 0.15	-0.30 ± 0.15	...	13
HD59360	0.13 ± 0.15	-0.16 ± 0.15	...	13
HD110989	0.11 ± 0.15	-0.25 ± 0.15	...	13
HD171620	-0.16 ± 0.15	-0.39 ± 0.15	...	13
HD121560	-0.13 ± 0.15	-0.38 ± 0.15	...	13
HD5065	0.12 ± 0.15	-0.12 ± 0.15	...	13
HD155646	0.27 ± 0.15	-0.03 ± 0.15	...	13
HD11007	-0.09 ± 0.15	-0.29 ± 0.15	...	13
HD153240	0.15 ± 0.15	-0.05 ± 0.15	...	13
HD191672	-0.16 ± 0.15	-0.38 ± 0.15	...	13
HD73400	0.00 ± 0.15	-0.17 ± 0.15	...	13
HD63333	-0.06 ± 0.15	-0.33 ± 0.15	...	13
HD15398	0.23 ± 0.15	0.02 ± 0.15	...	13
HD214576	-0.18 ± 0.15	-0.44 ± 0.15	...	13
HD107038	-0.21 ± 0.15	-0.33 ± 0.15	...	13
HD22718	0.15 ± 0.15	-0.13 ± 0.15	...	13
HD182758	-0.14 ± 0.15	-0.49 ± 0.15	...	13
HD186379	-0.11 ± 0.15	-0.33 ± 0.15	...	13
HD201444	-0.10 ± 0.15	-0.50 ± 0.15	...	13
HD216106	0.10 ± 0.15	-0.24 ± 0.15	...	13
HD159333	0.12 ± 0.15	-0.18 ± 0.15	...	13
HD153668	0.04 ± 0.15	-0.17 ± 0.15	...	13
HD153627	-0.04 ± 0.15	-0.30 ± 0.15	...	13
HD76349	-0.16 ± 0.15	-0.39 ± 0.15	...	13

Continued on next page

Table 6 – continued from previous page

ID	[O/H]	[S/H]	[B/H]	References
HD77408	-0.09 ± 0.15	-0.21 ± 0.15	...	13
HD26421	-0.03 ± 0.15	-0.32 ± 0.15	...	13
HD330	0.08 ± 0.15	-0.20 ± 0.15	...	13
HD210985	-0.21 ± 0.15	-0.46 ± 0.15	...	13
HD200580	-0.37 ± 0.15	-0.53 ± 0.15	...	13
HD22255	-0.01 ± 0.15	-0.22 ± 0.15	...	13
HD63332	0.21 ± 0.15	0.06 ± 0.15	...	13
HD88446	0.06 ± 0.15	-0.26 ± 0.15	...	13
HD69897	-0.05 ± 0.15	-0.20 ± 0.15	...	13
HD199085	0.03 ± 0.15	-0.10 ± 0.15	...	13
HD140750	0.14 ± 0.15	-0.26 ± 0.15	...	13
HD100446	-0.16 ± 0.15	-0.43 ± 0.15	...	13
HD149576	0.16 ± 0.15	-0.14 ± 0.15	...	13
HD126053	-0.16 ± 0.15	-0.34 ± 0.15	...	13
HD87838	-0.21 ± 0.15	-0.35 ± 0.15	...	13
HD219497	-0.07 ± 0.15	-0.42 ± 0.15	...	13
HD52711	0.05 ± 0.15	-0.16 ± 0.15	...	13
HD210718	-0.16 ± 0.15	-0.27 ± 0.15	...	13
HD140324	-0.01 ± 0.15	-0.28 ± 0.15	...	13
HD24421	-0.07 ± 0.15	-0.35 ± 0.15	...	13
HD136925	0.11 ± 0.15	-0.18 ± 0.15	...	13
HD101	-0.05 ± 0.15	-0.24 ± 0.15	...	13
HD218059	-0.02 ± 0.15	-0.24 ± 0.15	...	13
HD152986	0.06 ± 0.15	-0.12 ± 0.15	...	13
HD22521	0.03 ± 0.15	-0.21 ± 0.15	...	13
HD45067	0.07 ± 0.15	-0.09 ± 0.15	...	13
HD41640	-0.30 ± 0.15	-0.50 ± 0.15	...	13
HD204712	-0.04 ± 0.15	-0.38 ± 0.15	...	13
HD224233	0.07 ± 0.15	-0.12 ± 0.15	...	13
HD9670	-0.07 ± 0.15	-0.24 ± 0.15	...	13
HD108134	-0.06 ± 0.15	-0.32 ± 0.15	...	13
HD131599	-0.07 ± 0.15	-0.40 ± 0.15	...	13
HD127667	-0.13 ± 0.15	-0.34 ± 0.15	...	13
HD6840	-0.10 ± 0.15	-0.34 ± 0.15	...	13
HD167588	-0.08 ± 0.15	-0.33 ± 0.15	...	13
HD198089	0.00 ± 0.15	-0.24 ± 0.15	...	13
HD5750	-0.19 ± 0.15	-0.31 ± 0.15	...	13
HD193664	-0.02 ± 0.15	-0.17 ± 0.15	...	13
HD218637	-0.13 ± 0.15	-0.22 ± 0.15	...	13
HD221356	-0.15 ± 0.15	-0.25 ± 0.15	...	13
HD3454	-0.22 ± 0.15	-0.51 ± 0.15	...	13
HD16067	0.23 ± 0.15	-0.04 ± 0.15	...	13
HD91638	-0.03 ± 0.15	-0.24 ± 0.15	...	13
HD146946	-0.07 ± 0.15	-0.33 ± 0.15	...	13
HD204559	-0.04 ± 0.15	-0.32 ± 0.15	...	13
HD94835	0.24 ± 0.15	0.12 ± 0.15	...	13
HD198109	-0.15 ± 0.15	-0.41 ± 0.15	...	13
HD131039	0.18 ± 0.15	-0.14 ± 0.15	...	13
HD36066	0.16 ± 0.15	0.01 ± 0.15	...	13
HD5494	0.18 ± 0.15	-0.06 ± 0.15	...	13
HD210923	0.12 ± 0.15	-0.17 ± 0.15	...	13
HD212858	-0.10 ± 0.15	-0.39 ± 0.15	...	13
HD157466	-0.17 ± 0.15	-0.39 ± 0.15	...	13
HD220908	0.15 ± 0.15	-0.10 ± 0.15	...	13
HD3532	0.02 ± 0.15	-0.28 ± 0.15	...	13
HD109154	0.01 ± 0.15	-0.32 ± 0.15	...	13
HD174160	0.12 ± 0.15	-0.06 ± 0.15	...	13
HD102618	0.03 ± 0.15	-0.26 ± 0.15	...	13
HD86884	-0.01 ± 0.15	-0.24 ± 0.15	...	13

Continued on next page

Table 6 – continued from previous page

ID	[O/H]	[S/H]	[B/H]	References
HD223436	0.21 \pm 0.15	0.03 \pm 0.15	...	13
HD15029	-0.10 \pm 0.15	-0.28 \pm 0.15	...	13
HD6312	-0.04 \pm 0.15	-0.28 \pm 0.15	...	13
HD3440	-0.03 \pm 0.15	-0.30 \pm 0.15	...	13
HD214111	0.20 \pm 0.15	-0.05 \pm 0.15	...	13
HD100067	-0.11 \pm 0.15	-0.27 \pm 0.15	...	13
HD118687	-0.11 \pm 0.15	-0.38 \pm 0.15	...	13
HD218470	0.23 \pm 0.15	-0.07 \pm 0.15	...	13
HD102080	-0.14 \pm 0.15	-0.32 \pm 0.15	...	13
HD11592	-0.05 \pm 0.15	-0.27 \pm 0.15	...	13
HD220842	0.09 \pm 0.15	-0.24 \pm 0.15	...	13
HD11045	0.07 \pm 0.15	-0.25 \pm 0.15	...	13
HD106510	-0.16 \pm 0.15	-0.39 \pm 0.15	...	13
HD186408	0.21 \pm 0.15	0.06 \pm 0.15	...	13
HD204306	-0.13 \pm 0.15	-0.52 \pm 0.15	...	13
HD201835	-0.04 \pm 0.15	-0.28 \pm 0.15	...	13
HD3079	0.08 \pm 0.15	-0.16 \pm 0.15	...	13
HD210640	0.01 \pm 0.15	-0.28 \pm 0.15	...	13
HD163363	0.17 \pm 0.15	0.01 \pm 0.15	...	13
HD152449	0.16 \pm 0.15	-0.03 \pm 0.15	...	13
HD86560	-0.08 \pm 0.15	-0.37 \pm 0.15	...	13
HD101716	0.20 \pm 0.15	-0.11 \pm 0.15	...	13
HD216385	0.02 \pm 0.15	-0.15 \pm 0.15	...	13
HD89010	0.23 \pm 0.15	0.02 \pm 0.15	...	13
HD101676	-0.12 \pm 0.15	-0.37 \pm 0.15	...	13
HD139457	-0.11 \pm 0.15	-0.41 \pm 0.15	...	13
HD190681	0.17 \pm 0.15	-0.02 \pm 0.15	...	13
HD21922	-0.07 \pm 0.15	-0.41 \pm 0.15	...	13
HD99126	0.07 \pm 0.15	-0.10 \pm 0.15	...	13
HD20717	-0.11 \pm 0.15	-0.27 \pm 0.15	...	13
HD6250	0.06 \pm 0.15	-0.13 \pm 0.15	...	13
HD77134	-0.08 \pm 0.15	-0.26 \pm 0.15	...	13
HD97037	0.03 \pm 0.15	-0.12 \pm 0.15	...	13
HD130253	0.06 \pm 0.15	-0.16 \pm 0.15	...	13
HD124819	0.08 \pm 0.15	-0.22 \pm 0.15	...	13
HD70	-0.06 \pm 0.15	-0.27 \pm 0.15	...	13
HD85902	-0.17 \pm 0.15	-0.50 \pm 0.15	...	13
HD219476	-0.17 \pm 0.15	-0.46 \pm 0.15	...	13
HD217877	0.04 \pm 0.15	-0.14 \pm 0.15	...	13
HD223854	-0.24 \pm 0.15	-0.47 \pm 0.15	...	13
HD171886	0.00 \pm 0.15	-0.28 \pm 0.15	...	13
HD153	0.29 \pm 0.15	0.00 \pm 0.15	...	13
HD3894	-0.20 \pm 0.15	-0.35 \pm 0.15	...	13
HD214435	-0.07 \pm 0.15	-0.28 \pm 0.15	...	13
HD202884	-0.03 \pm 0.15	-0.22 \pm 0.15	...	13
HD54182	0.18 \pm 0.15	-0.16 \pm 0.15	...	13
HD112756	-0.13 \pm 0.15	-0.31 \pm 0.15	...	13
HD169359	-0.01 \pm 0.15	-0.23 \pm 0.15	...	13
HD225239	-0.10 \pm 0.15	-0.44 \pm 0.15	...	13
HD219983	0.02 \pm 0.15	-0.17 \pm 0.15	...	13
HD76272	-0.09 \pm 0.15	-0.35 \pm 0.15	...	13
HD219306	-0.01 \pm 0.15	-0.25 \pm 0.15	...	13
HD14877	-0.12 \pm 0.15	-0.36 \pm 0.15	...	13
HD201490	-0.04 \pm 0.15	-0.20 \pm 0.15	...	13
HD216631	-0.14 \pm 0.15	-0.41 \pm 0.15	...	13
HD148049	-0.08 \pm 0.15	-0.31 \pm 0.15	...	13
HD214557	0.21 \pm 0.15	0.02 \pm 0.15	...	13
HD201639	-0.32 \pm 0.15	-0.45 \pm 0.15	...	13
HD176796	0.00 \pm 0.15	-0.32 \pm 0.15	...	13

Continued on next page

Table 6 – continued from previous page

ID	[O/H]	[S/H]	[B/H]	References
HD195200	0.05 ± 0.15	-0.19 ± 0.15	...	13
HD23438	-0.02 ± 0.15	-0.29 ± 0.15	...	13
HD90878	0.15 ± 0.15	-0.19 ± 0.15	...	13
HD94012	-0.14 ± 0.15	-0.43 ± 0.15	...	13
HD27816	-0.25 ± 0.15	-0.47 ± 0.15	...	13
HD191649	0.06 ± 0.15	-0.18 ± 0.15	...	13
HD215442	0.28 ± 0.15	-0.11 ± 0.15	...	13
HD101472	0.11 ± 0.15	-0.15 ± 0.15	...	13
HD71148	0.07 ± 0.15	-0.07 ± 0.15	...	13
HD223583	-0.14 ± 0.15	-0.41 ± 0.15	...	13
HD8671	0.10 ± 0.15	-0.15 ± 0.15	...	13
HD6834	-0.30 ± 0.15	-0.53 ± 0.15	...	13
HD36909	0.08 ± 0.15	-0.18 ± 0.15	...	13
HD99984	-0.03 ± 0.15	-0.30 ± 0.15	...	13
HD912	0.17 ± 0.15	-0.18 ± 0.15	...	13
HD209320	0.16 ± 0.15	-0.10 ± 0.15	...	13
HD36667	-0.06 ± 0.15	-0.35 ± 0.15	...	13
HD156635	0.16 ± 0.15	-0.03 ± 0.15	...	13
HD194497	-0.07 ± 0.15	-0.26 ± 0.15	...	13
HD192145	-0.04 ± 0.15	-0.28 ± 0.15	...	13
HD160078	0.36 ± 0.15	-0.03 ± 0.15	...	13
HD99233	-0.24 ± 0.15	-0.54 ± 0.15	...	13
HD206860	0.10 ± 0.15	-0.10 ± 0.15	...	13
HD145937	-0.11 ± 0.15	-0.52 ± 0.15	...	13

DLAs				
J1340+1106	-1.65 ± 0.09	-1.85 ± 0.07	...	14
Q2059–360	-1.58 ± 0.10	-1.72 ± 0.09	...	15,16
Q0841+12	-1.32 ± 0.14	-1.45 ± 0.13	...	16,17
HE2243–6031	-1.15 ± 0.20	-0.94 ± 0.03	...	18
Q1337+113	-1.95 ± 0.12	-1.82 ± 0.08	...	16,19

ISM				
HD88115	0.03 ± 0.16	...	-0.28 ± 0.18	20
HD92554	0.03 ± 0.14	...	-0.35 ± 0.16	20
HD99890	0.25 ± 0.17	...	-0.41 ± 0.25	20
HD104705	0.01 ± 0.08	...	-0.42 ± 0.10	20
HD121968	0.02 ± 0.11	...	-0.51 ± 0.21	20
HD177989	0.05 ± 0.09	...	-0.53 ± 0.12	20

REFERENCES – (1) Smith et al. (2001). (2) Takeda (2007). (3) Brooks et al. (2002) and references therein. (4) Tan et al. (2010). (5) Caffau et al. (2005). (6) Venn et al. (2002) and references therein. (7) Daflon et al. (2009). (8) Nissen et al. (2007).. (9) Rich & Boesgaard (2009). (10) Spite et al. (2005). (11) Spite et al. (2011). (12) Ramírez et al. (2012). (13) Reddy et al. (2003) (14) Cooke et al. (2011). (15) Srianand et al. (2005). (16) Petitjean et al. (2008). (17) Dessauges-Zavadsky et al. (2007). (18) Lopez et al. (2002). (19) Prochaska et al. (2007). (20) Ritchey et al. (2011).